

# Effects of Sonic Line Transition on Aerothermodynamics of the Mars Pathfinder Probe

Peter A. Gnoffo and K. James Weilmuenster\*

and

Robert D. Braun and Christopher I. Cruz†

NASA Langley Research Center

Hampton, VA 23681-0001

## Nomenclature

### Abstract

Flowfield solutions over the Mars Pathfinder Probe spanning the trajectory through the Martian atmosphere at angles of attack from 0 to 11 degrees are obtained. Aerodynamic coefficients derived from these solutions reveal two regions where the derivative of pitching moment with respect to angle of attack is positive at small angles of attack. The behavior is associated with the transition of the sonic line location between the blunted nose and the windside shoulder of the 70 degree half-angle cone in a gas with a low effective ratio of specific heats. The transition first occurs as the shock layer gas chemistry evolves from highly nonequilibrium to near equilibrium, above approximately 6.5 km/s and 40 km altitude, causing the effective specific heat ratio to decrease. The transition next occurs in an equilibrium flow regime as velocities decrease through 3.5 km/s and the specific heat ratio increases again with decreasing enthalpy. The effects of the expansion over the shoulder into the wake are more strongly felt on the frustum when the sonic line sits on the shoulder. The transition also produces a counter-intuitive trend in which windside heating levels decrease with increasing angle of attack resulting from an increase in the effective radius of curvature. Six-degree-of-freedom trajectory analyses utilizing the computed aerodynamic coefficients predict a moderate, 3 to 4 degree increase in total angle of attack as the probe, spinning at approximately 2 revolutions per minute, passes through these regions.

$a$	speed of sound, m/s
$C_A$	axial force coef.
$C_D$	drag coef.
$C_L$	lift coef.
$C_m$	pitching moment coef.
$C_{m,\alpha}$	pitching moment coef. derivative, per radian
$C_N$	normal force coef.
$C_{v,tr}$	specific heat at constant volume including only translational and rotational capacities, J/kg-K
$D$	probe diameter, m
$h$	altitude, km
$M$	Mach number
$\mathcal{M}$	mixture molec. weight, kg/kg-mole
$p$	pressure, N/m <sup>2</sup>
$q$	convective heating, W/cm <sup>2</sup>
$Q$	dynamic pressure, N/m <sup>2</sup>
$r$	radius from probe axis, m
$Re$	Reynolds number
$\mathcal{R}$	univ. gas const., 8314.3 J/kg-mole-K
$T_\infty$	freestream temperature, K
$V_\infty$	freestream velocity, m/s
$x, y, z$	Cartesian coordinates, m
$\alpha$	angle of attack, degrees
$\alpha_T$	total angle of attack ( $\alpha^2 + \beta^2$ ) <sup>1/2</sup> , degrees
$\beta$	angle of yaw, degrees
$\gamma$	effective ratio of specific heats
$\rho$	density, kg/m <sup>3</sup>
$\eta$	equil. normal shock density ratio

---

\* Aerospace Engineer, Aerothermodynamics Branch, Gas Dynamics Division, Associate Fellow AIAA.

† Aerospace Engineer, Vehicle Analysis Branch, Senior Member AIAA

Copyright ©1995 by the American Institute of Aeronautics and Astronautics, Inc. No copyright is asserted in the United States under Title 17, U.S. Code. The U.S. Government has a royalty-free license to exercise all rights under the copyright claimed herein for Governmental purposes. All other rights are reserved by the copyright owner.

### Subscripts

$\infty$	freestream
$sh$	shoulder

## Introduction

The Mars Environmental Survey (MESUR)<sup>1</sup> Pathfinder<sup>2</sup> program proposes to observe the Martian atmosphere and surface with unmanned probes. Recently renamed Mars Pathfinder, the program, embracing the design principles “faster, better, cheaper”, now focuses on entry, descent and landing of a single probe. The design program naturally borrows much, including body shape, from the earlier Viking project<sup>3</sup> (and associated ground-based experimental data<sup>4-7</sup>), which landed a science station on the Martian surface in 1978. Unlike Viking, Pathfinder seeks to simplify the mission by utilizing direct entry into the Martian atmosphere and eliminating any reactive control system during its descent. The direct entry forces a higher entry velocity and heating rates than experienced by Viking. Aerodynamic stability is to be maintained at a nominal zero degree angle of attack with an on-axis center-of-gravity location while the probe spins at approximately two revolutions per minute.

While much of the research in support of the Viking project can be used for Pathfinder design validation, the differences in entry velocity and angle of attack necessitate a re-evaluation of Viking shape aerothermodynamics at Pathfinder conditions. Viking had been designed to fly at an eleven degree angle of attack, a condition for which the aerodynamic uncertainties associated with gas models at hypersonic conditions were relatively small for that shape. The primary goal of this paper is to provide understanding of the aerodynamics for the Viking shape near zero degrees angle of attack for the Pathfinder mission. It also demonstrates how heating distributions change as a function of angle of attack, and highlights the behavior of both the aerodynamic coefficients and heating distributions as a function of the sonic line location on the probe. The heating analysis contained herein is purposefully kept very simple; more comprehensive heating analyses which ignore the three-dimensional issues treated here may be found in the literature.<sup>8-15</sup>

To this end, a matrix of fast running, inviscid, perfect gas solutions is generated and aerodynamic coefficients are extracted. The matrix spans angles of attack from zero to eleven degrees and trajectory points from peak dynamic pressure to parachute deployment. The matrix includes velocities for which ballistic range tests indicated static stability problems with the Viking shape at small angles of attack. The perfect gas, constant specific heat ratio is chosen to match the equilibrium, normal shock density ratio at the specific freestream velocities and temperatures. Viscous, real gas solutions are concurrently generated on a complementary matrix to: (1) ascertain the sensitivity of blunt body aerodynamics to the simplified perfect gas solutions; (2) define probe aerodynamics in the nonequi-

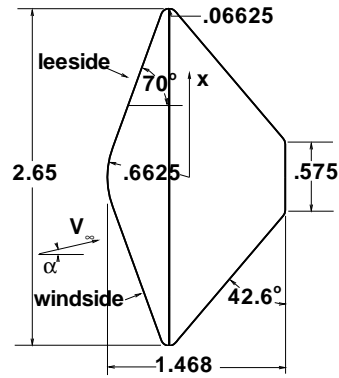


Figure 1: Diagram of the Mars Pathfinder probe.

librium flow regime prior to peak heating; and (3) establish the convective heating distributions. Limited validation of results is provided with grid convergence studies and comparison to experimental data.

## Configuration and Trajectory

The Mars Pathfinder configuration is shown in Fig. 1. The forebody is a  $70^\circ$  half angle cone with base diameter 2.65 m, nose radius 0.6625m and shoulder radius 0.06625 m. The on-axis center-of-gravity is located 0.662 m behind the nose. Only the forebody is included in this study unless otherwise specified. The forebody analysis is sufficient for computation of aerodynamic coefficients at hypersonic conditions. Baseflow effects are important to computation of aerodynamic coefficients at low supersonic conditions and will be briefly discussed.

A preliminary trajectory<sup>16</sup> is generated assuming a mass of 418 kg. and a 7.6 km/s ballistic entry at -18 degrees. Test points along this trajectory, defined in Table 1, range from 18 s prior to peak heating to parachute deployment.

## Algorithms

### Perfect Gas, Inviscid Analysis

The perfect gas, inviscid analysis is provided by the High ALpha Inviscid Solution (HALIS)<sup>17</sup> code. The code employs an explicit MacCormack predictor-corrector scheme. The bow shock defines the inflow boundary, on which the Rankine Hugoniot relations for

a moving shock define the inflow conditions. The inviscid wall boundary condition enforces the tangency condition on the surface and corrects velocities to enforce a constant total enthalpy. Backward differences are used on the outflow boundary, which lies downstream of the sonic line in a supersonic domain. High confidence in this code for inviscid, blunt body flow computations is derived from extensive comparisons as documented in the literature.<sup>18–20</sup>

The perfect gas analysis requires an approximation to real-gas chemistry behind the bow shock using an appropriate choice for the ratio of specific heats,  $\gamma$ . A standard approximation for air chemistry based on a local ratio of enthalpy to internal energy<sup>21</sup> causes some problems when used for Martian atmospheric gases because of the large, negative heat of formation for  $\text{CO}_2$ . An alternative approach used here is to choose a constant value for  $\gamma$  which matches the density ratio ( $\eta = \rho_2/\rho_1$ ) across a normal shock for equilibrium flow.

$$\gamma = \frac{\eta + 1}{\eta - 1} - \frac{2\eta}{(\eta - 1)M_\infty^2} \quad (1)$$

The values for  $\eta$  were computed using a viscous shock layer code<sup>12</sup> with free energy minimization for the Martian atmospheric chemistry. This approximation is only applied to points on the trajectory at or following peak dynamic pressure where the equilibrium normal shock density ratio was in good agreement with the nonequilibrium calculation discussed below. These effective values for  $\gamma$  in the equilibrium regime are presented in Table 1. Sound speed is calculated with the perfect gas relation:

$$a^2 = \gamma \frac{p}{\rho} \quad (2)$$

### Real Gas, Viscous Analysis

The real gas, viscous analysis is provided by the Langley Aerothermodynamic Upwind Relaxation Algorithm (LAURA).<sup>22–24</sup> Comparisons to experimental data for hypersonic flows in air are documented in the literature.<sup>25–29</sup> The code employs upwind-biased, point-implicit relaxation. Inviscid fluxes are approximated with Roe’s averaging,<sup>30</sup> eigenvalue limiting (similar to Harten<sup>31</sup>), and Yee’s symmetric total variation diminishing scheme.<sup>32</sup> Viscous fluxes are approximated with central differences. A recently added model for Martian atmospheric constituents includes 8 species ( $\text{CO}_2$ ,  $\text{CO}$ ,  $\text{N}_2$ ,  $\text{O}_2$ ,  $\text{NO}$ ,  $\text{C}$ ,  $\text{N}$ ,  $\text{O}$ ).<sup>14</sup> Reacting gas chemistry is used for the hypersonic cases (Mach 9 and above). The code is sufficiently robust to achieve convergence at near equilibrium conditions. Frozen chemistry is employed for the Mach 1.9 case because the post shock conditions are not severe enough to induce chemical reactions. Thermal equilibrium is specified for all points below peak dynamic pressure (Mach 22.3). A two-temperature model is applied at trajectory points

prior to and including peak dynamic pressure. The local Mach number is based on a frozen (species, vibration, electronic excitation) sound speed:<sup>33</sup>

$$a^2 = \left(1 + \frac{\mathcal{R}}{C_{v, tr} \mathcal{M}}\right) \frac{p}{\rho} \quad (3)$$

Unlike HALIS, LAURA employs shock capturing and the inflow boundary and grid are aligned with the captured bow shock. No-slip conditions are applied in a pseudo cell behind the surface within the context of a finite-volume formulation. Wall temperatures are held constant and defined in Table 1. Species mass fractions at the wall are held fixed at their respective freestream values ( $c_{\text{CO}_2} = .97$ ,  $c_{\text{N}_2} = .03$ , all others set to  $10^{-10}$ ). Extrapolation is used to close the outflow boundary.

LAURA can be used to generate inviscid, perfect gas solutions. However, the wall boundary conditions in this mode are very simple, specifying zero normal mass flux and extrapolating pressure and energy to the wall with no corrections for total enthalpy conservation. Nevertheless, LAURA is used in an inviscid, perfect gas mode to ascertain sensitivity of the solution for aerodynamic coefficients to algorithm at selected trajectory points. The differences are small and will be discussed.

### Computational Grid

The HALIS solutions are generated on a cylindrically derived coordinate system with the axis coincident with the vehicle axis. The surface grid (Fig. 2a) uses 46 points in the radial (predominantly stream-wise) direction and 36 points in the circumferential direction. The volume grid is built up in a body normal direction using 21 points between the surface and the bow shock.

The surface-grid distribution for the LAURA test cases (Fig. 2b) derives from a singularity free mapping that provides a nearly uniform mesh in the stagnation region and enhanced circumferential and axial resolution at the shoulders of generic aerobrake shapes. The surface grid may be perceived as a rectangular sheet which has one boundary on the symmetry plane and the other three boundaries stretched along the outer edge of the vehicle. Grid lines in the vicinity of the two sheet corners on the circular shoulder are somewhat skewed. The baseline grid is defined by 61 x 31 point rectangle which yields 61 points along the symmetry plane and 121 points along the outer, semi-circular edge. The volume grid is built up in a body normal direction using 65 points between the surface and the inflow boundary which lies upstream of the captured bow shock. The normal distribution is defined with a

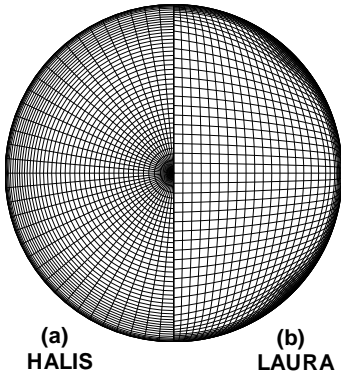


Figure 2: Forebody surface grid on the Mars Pathfinder probe.

cell Reynolds number equal to 1 at the surface and a stretching function in which roughly half the available cells are assigned to the boundary layer and the remainder are equally spaced across the shock layer.<sup>34</sup> Normal grid distribution is periodically updated as the solution evolves. Some grid refinement studies are implemented using an 81 x 41 point surface grid.

Differences in the treatment of the bow shock preclude use of the same grid for both solution techniques. Both grid structures emphasize resolution in the vicinity of the circular shoulder because details of the expansion process are critical to the evaluation of aerodynamic coefficients. The rectangular topology, though more difficult to generate, is superior to the cylindrical topology for the purpose of resolving pressure and heating distributions around the vehicle axis, unencumbered by the presence of a coordinate singularity.

## Aerodynamics

### HALIS: Inviscid, Perfect Gas Aerodynamics

The inviscid, perfect-gas solution matrix run with the HALIS code and the associated aerodynamic coefficients are presented in Table 2. The matrix includes angles of attack of  $0^\circ$  (design condition),  $2^\circ$ ,  $5^\circ$ ,  $8^\circ$ , and  $11^\circ$  (Viking condition). A base pressure equal to  $p_\infty$  is assumed in the computation of aerodynamic coefficients.

Lift, drag, and pitching moment coefficients are plotted as a function of Mach number in Fig. 3 with the solid lines and filled symbols. Recall that the effective specific heat ratio  $\gamma$  also varies with Mach number, so that gas chemistry effects are approximately included in these results. The lift coefficient is insensitive to Mach number for this configuration above Mach

6. The drag coefficient shows a stronger dependence on Mach number. The pitching moment coefficient shows a distinct hump (local maximum) as a function of Mach number and the location of the hump changes with angle of attack.

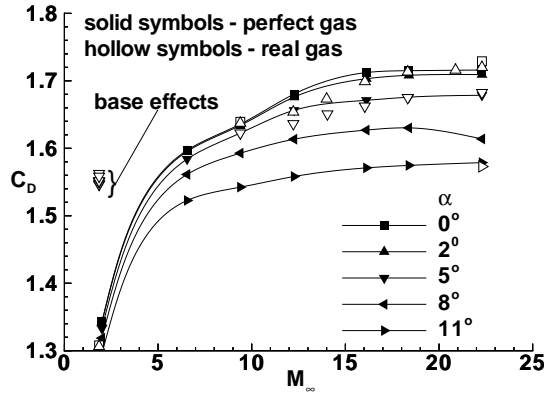
### LAURA: Viscous, Reacting Aerodynamics

The local maxima noted in the HALIS results suggests the possibility that the the pitching moment may be positive at small angles of attack near Mach 12 in which case the vehicle would be statically unstable. Concern regarding this feature prompted an expanded test matrix for the viscous, real-gas solutions using LAURA. The test conditions and associated aerodynamics are presented in Table 3. Lift, drag, and pitching moment coefficients are plotted as a function of Mach number in Fig. 3 with the hollow symbols. These results include viscous forces. Aerodynamic coefficient magnitudes including unsteady baseflow effects (to be discussed subsequently) at Mach 1.9 and 5 degrees angle of attack are indicated by the open symbols within the bracket labelled base effects. The LAURA and HALIS predictions for lift coefficient are in excellent agreement for all Mach numbers and angles of attack tested. The LAURA and HALIS predictions for drag and pitching moment coefficient begin to diverge above Mach 9. The maximum percent difference in drag coefficient, 1.3%, occurs in the test matrix at Mach 12,  $\alpha = 2^\circ$ . The maximum difference in pitching moment coefficient, 0.00245, occurs at Mach 16,  $\alpha = 2^\circ$ . The LAURA results predict static instability at this Mach number for small angles of attack.

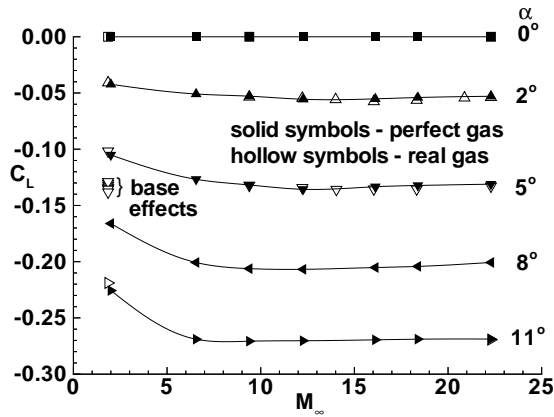
The ratio of pitching moment to normal coefficient is related to a nondimensional stability margin. This ratio, plotted in Fig. 4, collapses for all angles of attack in the test matrix below Mach 10 into a straight line. (Baseflow effects at Mach 1.9 are not included in these curves.) Above Mach 20, the angle of attack dependence diminishes again (until nonequilibrium effects become important as discussed in the next section). In between, mechanisms operate which are clearly sensitive to both Mach number (gas chemistry) and angle of attack.

### Pressure and Moment Distributions

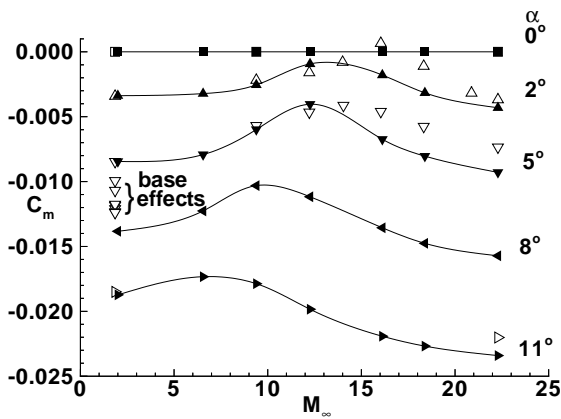
At small angles of attack, both  $C_m$  and  $C_N$  are small numbers whose magnitude depend on the difference of large windside and leeside forces. (The term leeside is somewhat of a misnomer; it refers to the side of the probe pitched away from the oncoming flow even though direct impingement still occurs.) To better understand how these windside and leeside forces evolve to produce the static instability at  $\alpha = 2^\circ$ , pressure distributions on the symmetry plane are presented in



(a) Drag coefficient



(b) Lift coefficient



(c) Pitching moment coefficient

Figure 3: Aerodynamic coefficients versus Mach number at several angles of attack  $\alpha$  for predominantly equilibrium flow regime below  $M_\infty = 22.3$ , maximum dynamic pressure.

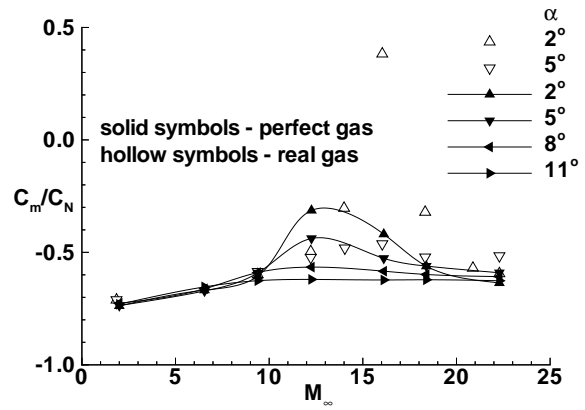


Figure 4: Ratio of pitching moment coefficient to normal force coefficient versus Mach number at several angles of attack  $\alpha$  for predominantly equilibrium flow regime.

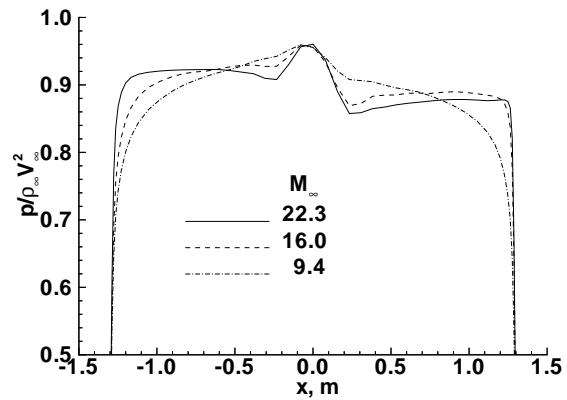


Figure 5: Pressure distribution along the symmetry plane for three Mach numbers spanning the static instability at  $\alpha = 2^\circ$  in the predominantly equilibrium gas chemistry regime.

Fig. 5 at trajectory points before the static instability ( $M_\infty = 22.3$ ), at the peak of the static instability ( $M_\infty = 16.0$ ), and after the static instability ( $M_\infty = 9.4$ ). On the leeside ( $x > 0.5$ ) the pressure for  $M_\infty = 22.3$  has a relatively constant, positive slope all the way to the circular shoulder ( $x = 1.28$ ) at which point it drops sharply in the expansion to the wake. The nondimensional pressure at  $M_\infty = 16.0$  is approximately 1.5 % higher than at  $M_\infty = 22.3$  but shows an earlier and more moderate expansion. At  $M_\infty = 9.4$  the pressure distribution has a stronger, negative slope and the pressure drop at the shoulder feeds far upstream. On the windside ( $x < -0.5$ ) the pressure distribution starts relatively flat at  $M_\infty = 22.3$  with some upstream influence of the shoulder evident in the rounded drop at  $x = -1.28$ . The flat distribution becomes more rounded, and average windside nondi-

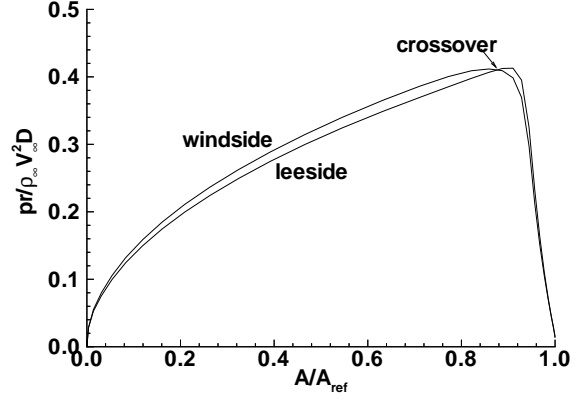
mensional pressure levels continue to decrease with decreasing Mach number as the effects of the expansion feed farther upstream.

Though not easily seen, there is a small region near the shoulder where the leeside pressure exceeds the corresponding windside pressure for the two highest Mach numbers. The behavior of the pressure distribution in this region significantly influences the pitching moment coefficient because of the relatively larger moment arms and surface area at the edge of the probe as compared to the inboard nose and fustrum regions. The integrated effect of pressure on  $C_m$  at  $\alpha = 2^\circ$  is approximately illustrated in Fig. 6 in which the product of pressure and moment arm (radius) is plotted as a function of area on the windside and leeside symmetry plane for  $M_\infty = 22.3$ , 16.0, and 9.4, respectively. The integrated area under each curve,  $\int prdA$ , represents the pitch up moment (destabilizing) caused by leeside pressures and the pitch down moment (stabilizing) caused by windside pressures. The difference in the areas represents the net pitching moment. In all cases, the small value of  $\alpha$  dictates that the difference of the integrated areas will be small. However, as noted earlier, a crossover point occurs in the curves at the two highest Mach numbers (Figs. 6a and 6b). At  $M_\infty = 16.0$  (Fig. 6b) the crossover occurs far enough inboard such that the leeside integrated area exceeds the windside integrated area, resulting in a net positive pitching moment.

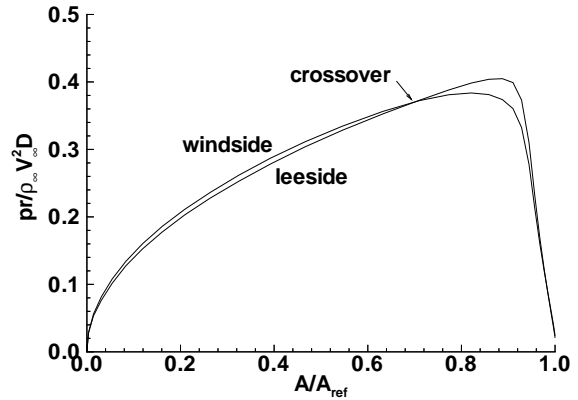
#### Influence of Sonic Line Location and $\gamma$

Direct influence of the expansion over the shoulder on the cone fustrum pressure levels further upstream is regulated by the magnitude of the local Mach number, and limited completely to the subsonic zone bounded by the sonic line. Acoustic waves cannot travel upstream in a supersonic flow. An exploded view of the sonic line location over the cone fustrum and circular shoulder is presented in Fig. 7a (leeside) and in Fig. 7b (windside). At  $M_\infty = 22.3$  the leeside sonic line lies along the boundary layer edge, essentially eliminating upstream influence of the expansion, consistent with observations in Fig. 5. At  $M_\infty = 16.0$  the leeside sonic line moves further out into the inviscid flow. A secondary subsonic bubble forms above the first in the inviscid layer, its upper boundary embedded in the captured shock. At  $M_\infty = 9.4$  the leeside sonic line terminates in a line nearly perpendicular to the shoulder, providing ample communication of the expansion to the entire shock layer as was evident in Fig. 5.

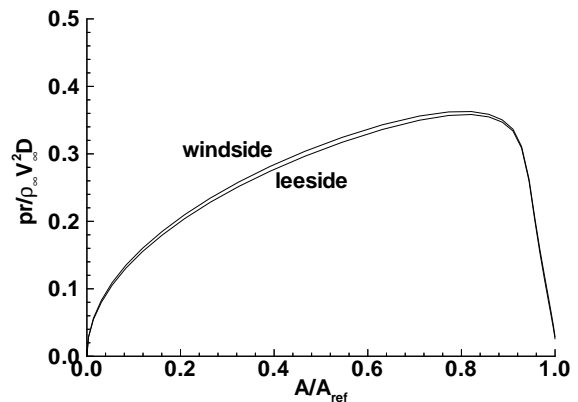
The windside sonic lines in Fig. 7b all terminate at lines above the shoulder which curve sharply downstream into the boundary layer in the rapidly expanding flow. The upper boundary of the windside sonic lines are embedded in the captured shock, and indicate



(a)  $M_\infty = 22.3$

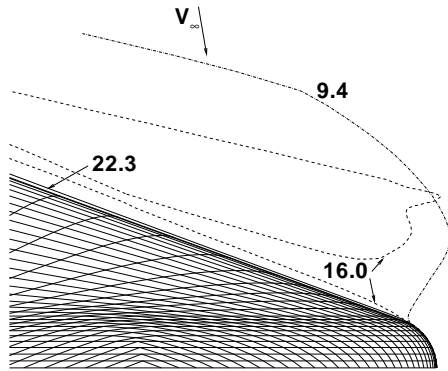


(b)  $M_\infty = 16.0$

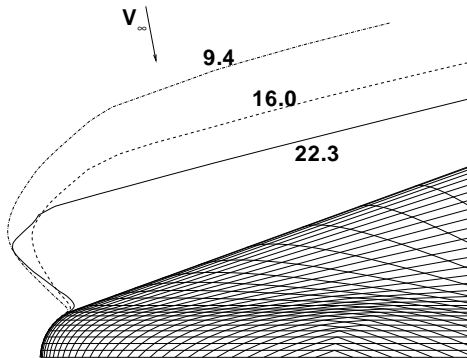


(c)  $M_\infty = 9.4$

Figure 6: Approximation to the pitching moment coefficient integral in the vicinity of the leeside and windside symmetry planes at  $\alpha = 2^\circ$ .



(a) Leeside.



(b) Windside - upper portion of sonic line is embedded in the captured shock.

Figure 7: Sonic line location in the symmetry plane above the shoulder and cone fustrium for three Mach numbers spanning the static instability at  $\alpha = 2^\circ$  in the predominantly equilibrium gas chemistry regime. Flow enters from the top of the figure.

the significant influence of gas chemistry on shock layer thickness across this Mach number range. The size of the windside subsonic zone at  $M_\infty = 9.4$  is over twice as large as the subsonic zone at  $M_\infty = 22.3$ , and the windside pressures in Fig. 5 again confirm that the larger subsonic zone yields larger pressure relief over the windside cone fustrium.

The HALIS (perfect gas) predictions for sonic line location are not shown here, but they exhibit essentially the same behavior and relationship with pressure distribution as predicted by LAURA. Furthermore, the HALIS solutions are in reasonable agreement with predictions made by South<sup>35</sup> which define the pointed cone half angle for which the sonic line first moves to the corner as a function of  $\gamma$  and  $M_\infty$  in a perfect gas at  $\alpha = 0$ . (For pointed cone half angle of  $70^\circ$  the sonic line sits over the shoulder for  $\gamma > 1.09$  and  $M_\infty > 10$ . For pointed cone half angle of  $68^\circ$  the sonic line sits over the shoulder for  $\gamma > 1.12$  and  $M_\infty > 10$ .) The major differences between the HALIS and LAURA predictions are that no secondary subsonic bubbles are observed with HALIS and the pitching moment coefficient is negative in all cases. (It may be that a constant  $\gamma$  solution cannot sustain the results observed in the reacting gas case.)

It should be emphasized that, although Mach number has been used as a traditionally convenient, defining parameter in these cases, the gas chemistry effect on aerodynamics is more appropriately defined in terms of freestream velocity. For hypersonic flows, the post-shock conditions over blunt bodies are a function of velocity and density in the freestream, and are nearly independent of temperature for the range of conditions typically encountered in atmospheric flight. Consequently, the use of Mach number introduces an inappropriate freestream temperature dependence.

### Baseflow Effects on Aerodynamics

The baseflow computation is not time accurate, but relaxation with small, constant time step  $\Delta t = .001r_{max}/V_\infty$  yields time like variation. Baseflow computations at  $M_\infty = 22.3$  show no significant effect on aerodynamics where base pressure levels are approximately 0.6% of forebody levels. (Pressure across the base varied from 2.5 to 4.0 times freestream pressure.) These levels translate into a decrement of 0.0064 in  $C_A$  at  $\alpha = 5^\circ$ . However, significant influence is evident at  $M_\infty = 1.9$  in Fig. 3. Unsteady recirculation patterns cause a variation in aerodynamic coefficients bounded by the bracketed label in these figures. In this case, base pressure levels are approximately 10% of forebody pressure levels.

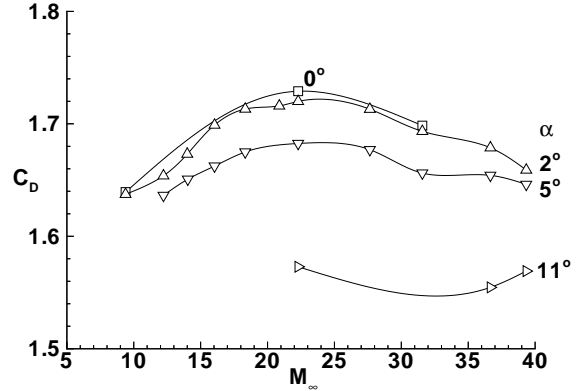
## Aerodynamics in Nonequilibrium Flow Regime

The effective ratio of specific heats  $\gamma$  increases with decreasing velocity, causing a transition in the sonic line location across the leeside fustrum at small angles of attack in an equilibrium flow regime for the Mars Pathfinder probe. This transition may also be expected to occur earlier in the trajectory as the post shock gas chemistry changes from frozen to equilibrium and  $\gamma$  decreases. In this range, the equilibrium post shock density ratio is inappropriate for defining an effective  $\gamma$ ; consequently, there are no perfect gas computations offered. Lift, drag, and pitching moment coefficients, including laminar shear forces, are plotted as a function of Mach number in Fig. 8 over the hypersonic range beginning 18 seconds prior to peak heating ( $M_\infty = 39$ ) and ending at  $M_\infty = 9.4$ . These results show both a slight decrease in axial force coefficient and a region of positive pitching moment coefficient at small  $\alpha$  for the nonequilibrium flow domain prior to the peak dynamic pressure point. The trends are consistent with sonic line transition discussed previously. The decrease in axial force is associated with the pressure drop at the shoulder feeding upstream in the large subsonic zone. All of the cases at  $\alpha = 2^\circ$  with positive pitching moment exhibit the leeside sonic line pattern that includes the secondary, subsonic bubble. This bubble sits above the primary sonic line that stretches along the boundary layer edge and attaches to the bow shock in front of the nose.

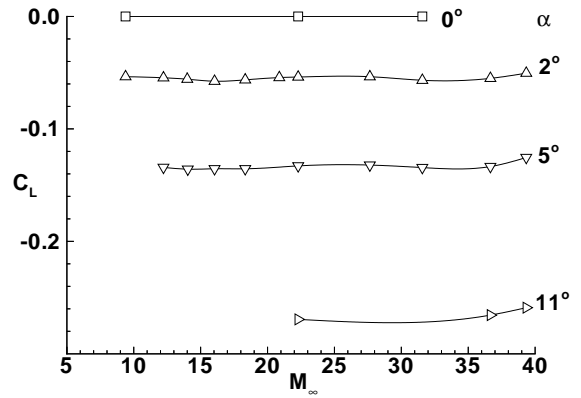
### Comparisons to Experimental Data

The Pathfinder probe forebody shape is very similar to the Viking Probe shape. Only the shoulder radii differ ( $r_{sh,Pathfinder} = 0.025D_{Pathfinder}$  and  $r_{sh,Viking} = .007D_{Viking}$ ). Although there are no experimental data available for aerodynamics of the Pathfinder shape, there are ballistic range data for the Viking shape obtained in  $CO_2$ . Data sets for  $C_D$  and  $C_{m,\alpha}$  presented in Figs. 9 and 10 are taken from Intrieri, et. al.<sup>4</sup> Conditions for this test are  $V_\infty \approx 3.4\text{km/s}$  and  $Re_{D,\infty} \approx 0.8 \times 10^6$ . These conditions are very close to the  $M_\infty = 16.0$  and  $14.0$  points in Table 1 for Pathfinder. Comparisons in Fig. 9 show that the predicted values for the Pathfinder  $C_D$  are within approximately 1% of experimental data for the Viking shape for  $\alpha < 10^\circ$ . Comparisons in Fig. 10 show that in this velocity range both experiment and calculation indicate a positive moment coefficient at small angles of attack. (No correction is made here for the different center-of-gravity reference point for the Viking model.)

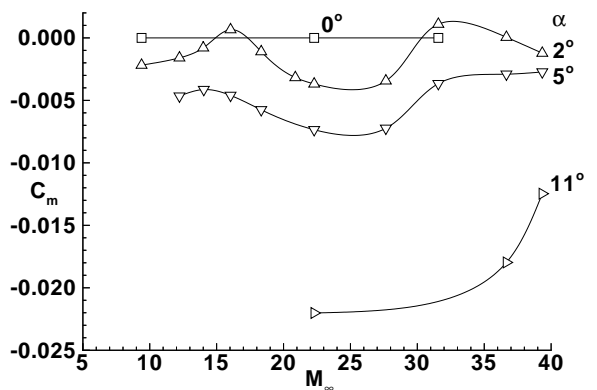
A calculation for the Viking shape corresponding to the experimental conditions of Intrieri, et. al.<sup>4</sup> was



(a) Drag coefficient



(b) Lift coefficient



(c) Pitching moment coefficient

Figure 8: Aerodynamic coefficients versus Mach number at several angles of attack  $\alpha$  for both hypersonic nonequilibrium and equilibrium flow regimes.

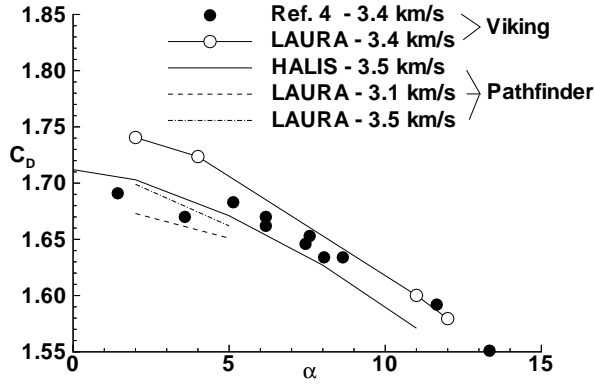


Figure 9: Comparison of computed drag coefficient for Mars Pathfinder probe with measured value for geometrically similar probe obtained in ballistic range with  $\text{CO}_2$ .

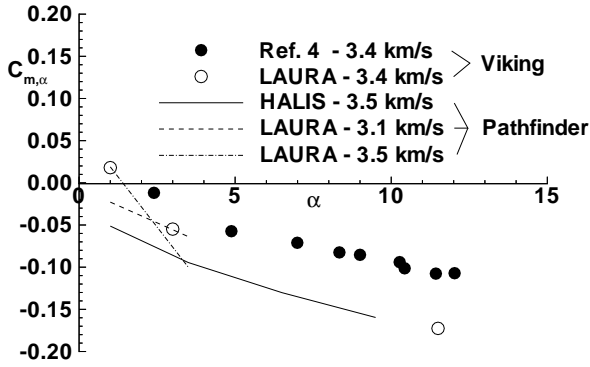


Figure 10: Comparison of computed pitching moment coefficient for Mars Pathfinder probe with measured value for geometrically similar Viking probe obtained in ballistic range with  $\text{CO}_2$ .

made to better validate the Pathfinder results, removing the small differences associated with geometry, velocity, Reynolds number, and center of gravity (cg). The results are shown as open circles in Fig. 9 for  $C_D$  and in Fig. 10 for  $C_{m,\alpha}$ . As noted earlier, all computations assume average base pressure equal to  $p_\infty$ . The effect of higher base pressures will tend to lower  $C_D$  ( $\Delta C_D = -0.02$  for  $p_{base} = 3p_\infty$ ). The pitching moment derivative is in good agreement with ballistic range data at small angles of attack but is approximately 50% more negative at  $\alpha = 11.5^\circ$ . Reasons for this discrepancy are not understood, particularly since LAURA computations of  $C_{m,\alpha} = -0.213$  and  $C_A = 1.617$  at  $\alpha = 11.5^\circ$  are in good agreement with flight data<sup>3</sup>  $-0.21 < C_{m,\alpha} < -0.17$  and  $1.61 < C_A < 1.68$  at conditions approximating peak dynamic pressure ( $V_\infty = 3.4$  km/s and  $\rho_\infty = 0.00098$

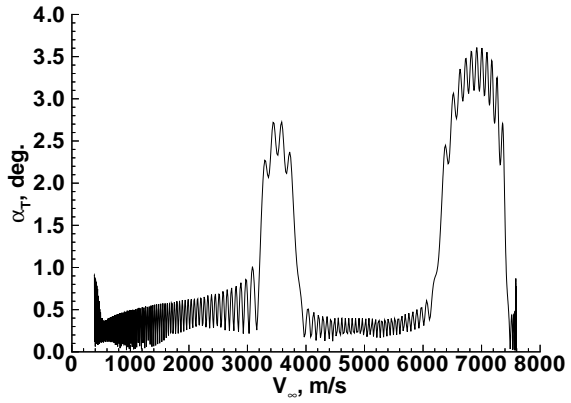


Figure 11: Total angle of attack as a function of velocity along the trajectory as determined from a six-degree-of-freedom trajectory analysis using aerodynamic coefficients computed by LAURA.

$\text{kg/m}^3$ ). (The specified cg location is 0.23 diameters behind the nose and 0.01326 diameters off axis for flight conditions.) The sensitivity of pitching moment coefficient to velocity (which affects sonic line location through the variation of  $\gamma$ ) for Pathfinder at  $\alpha < 5^\circ$  is clearly evident Fig. 10.

### Six-Degree-of-Freedom Trajectory

The total angle-of-attack  $\alpha_T$  (root-mean-square of  $\alpha$  and  $\beta$ ) as a function of velocity for the Mars Pathfinder probe is presented in Fig. 11 for a representative entry. This data was produced through integration of the six degree-of-freedom equations of motion with the Program to Optimize Simulated Trajectories using the LAURA aerodynamics and a Mars-GRAM atmosphere.<sup>36</sup> The probe begins its descent at 125 km with a relative velocity of 7.6 km/sec and a flight path angle of  $-14.8$  deg. For this trajectory, a ballistic coefficient of  $60$   $\text{kg/m}^2$  is assumed. Entry is initiated with zero degree total angle-of-attack and a roll rate of 2 rpm. Because the center-of-gravity is assumed to be on the symmetry axis, a nominal trim angle of zero degrees is expected. However, as shown in Fig. 11, throughout the two instability regions, significant attitude dispersions occur (with rms values of 3-4 deg). A more detailed examination of the Mars Pathfinder six degree-of-freedom flight dynamics using LAURA aerodynamics has been presented.<sup>37</sup>

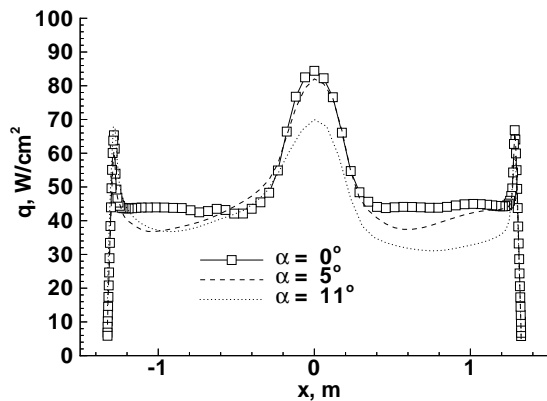


Figure 12: Surface heating distributions on symmetry plane for several angles of attack  $\alpha$  at the peak dynamic pressure point  $M_\infty = 22.3$ . The windside domain is defined by  $x < 0$ .

### Convective Heating

Convective heating distributions along the symmetry plane at  $M_\infty = 22.3$  (peak dynamic pressure trajectory point) are presented in Fig. 12. Simple boundary conditions include wall temperature set to 2000 K and species recombine to freestream mass fractions at the wall. There is no ablation or turbulence modelling. The maximum momentum thickness Reynolds number computed from the laminar profile is approximately 575 at peak dynamic pressure, occurring just upstream of the shoulder.

Note that both windside and leeside heating levels decrease with increasing angle of attack. At  $M_\infty = 22.3$  and  $\alpha = 0^\circ$  the sonic line runs along the boundary layer edge, with a very slender subsonic bubble sitting behind the captured shock above the fustum. The predicted stagnation point heating levels at  $\alpha = 0$  are in good agreement (approximately 8%)<sup>14</sup> with the Sutton and Graves correlation<sup>38</sup> for sphere in equilibrium flow using nose radius as a scale factor. This good agreement indicates that stagnation point velocity gradients are only weakly influenced by the presence of the cone. At larger angles of attack, the presence of the cone on the windside appears to have stronger influence on stagnation point gradients, lowering the heating levels because the effective body radius increases.

Even though heating decreases with increasing angle of attack, it should be noted that drag coefficient also decreases. The probe does not decelerate as effectively. Consequently, the peak heating and dynamic pressure points will occur later in the trajectory, possibly resulting in more severe aerothermal loads on the vehicle if it flies at non-zero angle of attack.

### Numerical Issues

The first two blocks of Table 4 show the effect of increasing surface grid resolution by 75%. The change in  $C_A$  is less than 0.25%. Changes in  $C_N$  and  $C_m$  are 16% and 33% respectively for the  $M_\infty = 16$  point at  $\alpha = 2^\circ$ . These values are more sensitive to grid because they represent the difference of two large, nearly equal contributions from the windside and leeside of the probe. Note, however, that these changes are relatively small (2.9% and 6.3%, respectively) when measured relative to the change in value going from  $\alpha = 2^\circ$  to  $\alpha = 5^\circ$ .

The contribution of viscous forces to the aerodynamics at small angles of attack are very small over most of the trajectory, as would be expected for a blunt body. The integration of only the pressure force contribution to aerodynamics is presented in the second and third blocks of Table 4 for two representative points.

Differences between the LAURA and HALIS results are predominantly due to the gas model. This sensitivity may be confirmed by examining the fourth and fifth blocks of Table 4. If LAURA is run in an inviscid, perfect gas mode like HALIS, then the differences in solution are algorithmic in nature. For the two representative points tested at  $\alpha = 5^\circ$ , differences in sensitive quantities like  $C_m$  for the two perfect gas solutions are less than 4% at  $M_\infty = 22.3$  and less than 10% at  $M_\infty = 16.0$ . When the real gas model and viscous terms are included in LAURA, the effects on aerodynamics are much larger (24% at  $M_\infty = 22.3$  and 25% at  $M_\infty = 16.0$ ). Since viscous contributions have already been shown to be negligible, the sensitivity of aerodynamics on the gas model is established.

### Conclusions

(1) As the Mars Pathfinder probe descends through the Martian atmosphere the minimum value of the post-shock effective  $\gamma$  first decreases from frozen gas chemistry values ( $\approx 1.333$ ) to equilibrium values (1.094) corresponding to a velocity of 4.86 km/s. As the probe continues to decelerate through an equilibrium post-shock gas chemistry regime, the value of  $\gamma$  increases again, until reaching its perfect gas value of 1.333 at parachute deployment (0.42 km/s).

(2) At small angles of attack ( $\alpha < 5^\circ$ ) the sonic line location shifts from the shoulder to the nose cap and back again on the leeside symmetry plane because of the change in  $\gamma$  and the cone half-angle of  $70^\circ$ . A noteworthy aspect of this transition process is the for-

mation of a secondary, subsonic zone over the leeside fustrum.

(3) Pressure distributions on the cone fustrum approaching the shoulder tend to be very flat when the sonic line sits forward over the spherical nose. Effects of the expansion over the shoulder can only be communicated upstream through the subsonic portion of the boundary layer. In contrast, pressure distributions on the cone fustrum approaching the shoulder tend to be more rounded when the sonic line sits on the shoulder, exhibiting a more pronounced influence of the expansion on the upstream flow.

(4) In general, windside pressures exceed leeside pressures on the cone fustrum, producing a stabilizing moment that pitches the probe back to zero angle of attack. However, the behavior of the pressure distribution in the vicinity of the shoulder significantly influences the pitching moment coefficient because of the relatively larger moment arms and surface area at the edge of the probe as compared to the inboard nose and fustrum regions. For the Mars Pathfinder probe at  $2^\circ$  angle of attack, the flat, leeside pressures approaching the shoulder (when the sonic line sits over the nose) can exceed the rounded windside pressures approaching the shoulder (when the sonic line sits over the shoulder). The net effect of this crossover distribution near the shoulder tends to pitch the probe to higher angles of attack. The overall balance (crossover-point location) is sensitive to both freestream conditions and the gas chemistry. The combination of small angle of attack, large cone angle, windside sonic line over the shoulder, and leeside sonic line over the nose with a secondary, subsonic zone above the leeside fustrum yield conditions which favor (but do not necessarily guarantee) a destabilizing pitching moment.

(5) Conditions for a positive, destabilizing moment coefficient derivative  $C_{m,\alpha}$  occur twice in the Mars Pathfinder mission as determined by the most accurate flow simulation used in this study. The first occurrence ( $7.5 > V_\infty > 6.5$  km/s,  $51 > h > 37$  km, vicinity of peak heating for this trajectory) results from the transition in the sonic line location as a function of gas chemistry changing from nonequilibrium to equilibrium. The second occurrence ( $4.0 > V_\infty > 3.1$  km/s,  $25 > h > 22$  km) results from the transition in the sonic line location as a function of decreasing flow enthalpy in an equilibrium gas chemistry regime.

(6) Sonic line movement affects the heating distributions by altering the effective radius of curvature of the body. Peak heating tends to decrease as angle of attack increases for fixed freestream conditions on the Mars Pathfinder probe because the body appears blunter to the oncoming flow. However, the drag coefficient decreases with increasing angle of attack, so that the ballistic coefficient increases and peak heating point along the trajectory may be more severe.

(7) A sample, six-degree-of-freedom trajectory based on the computed aerodynamics and a spin rate of 2 revolutions per minute predicts a precessing motion during the two, statically unstable periods in which the root-mean-square value of angle of attack is between 3 and 4 degrees.

## References

- <sup>1</sup>Hubbard, G. S., Wercinski, P. F., Sarver, G. L., Hanel, R. P., and Ramos, R., "A Mars Environmental Survey (MESUR) - Feasibility of a Low Cost Global Approach," IAF Paper 91-432, October 1991.
- <sup>2</sup>Bourke, R. D., Golombek, M. P., Spear, A. J., and Sturms, F. M., "MESUR and Its Role in an Evolutionary Mars Exploration Program," IAF Paper 92-0509, September 1992.
- <sup>3</sup>Inogoldby, R. N., Michel, F. C., Flaherty, T. M., Doty, M. G., Preston, B., Villyyard, K. W., and Steele, R. D., "Entry Data Analysis for Viking Landers 1 and 2," NASA CR 159388, November 1976.
- <sup>4</sup>Intrieri, P. F., Rose, C. E. D., and Kirk, D. B., "Flight Characteristics of Probes in the Atmospheres of Mars, Venus and the Outer Planets," *Acta Astronautica*, Vol. 4, 1977, pp. 789-799.
- <sup>5</sup>Sammonds, R. I., and Kruse, R. L., "Viking Entry Vehicle Aerodynamics at  $M = 2$  in Air and Some Preliminary Test Data for Flight in  $CO_2$  at  $M = 11$ ," NASA TN D-7974, June 1975.
- <sup>6</sup>Krumins, M. V., "Drag and Stability of Various Mars Entry Configurations," IAF Paper RE 138, October 1968.
- <sup>7</sup>Blake, W. W., "Experimental Aerodynamic Characteristics of the Viking Entry Vehicle Over the Mach Range 1.5 - 10.0," Martin Marietta TR-3720106, April 1971.
- <sup>8</sup>Papadopoulos, P., Tauber, M., and Chang, I. D., "Aerobraking in a Dusty Martian Atmosphere," AIAA Paper 90-1700, June 1990.
- <sup>9</sup>Chen, Y. K., Henline, W. D., Stewart, D. A., and Candler, G. V., "Navier-Stokes Solutions with Surface Catalysis for Martian Atmospheric Entry," *Journal of Spacecraft and Rockets*, Vol. 30, No. 1, January-February 1993, pp. 32-42.
- <sup>10</sup>Tauber, M., Henline, W., Chargin, M., Papadopoulos, P., Chen, Y., Yang, L., and Hamm, K., "MESUR Probe Aerobrake Preliminary Design Study," *Journal of Spacecraft and Rockets*, Vol. 30, No. 4, July-August 1993, pp. 431-437.
- <sup>11</sup>Candler, G. V., "Computation of Thermochemical Nonequilibrium Martian Atmosphere Entry Flows," AIAA Paper 90-1695, June 1990.
- <sup>12</sup>Gupta, R. N., Lee, K. P., Moss, J. N., and Sutton, K., "A Viscous-Shock-Layer Analysis of the Mar-

- tian Aerothermal Environment,” AIAA Paper 91-1345, June 1991.
- <sup>13</sup>Gupta, R. N., “An Aerothermal Study of the MESUR Pathfinder Aeroshell,” AIAA Paper 94-2025, June 1994.
- <sup>14</sup>Mitchletree, R. A., “Aerothermodynamic Methods for a Mars Environmental Survey Mars Entry,” *Journal of Spacecraft and Rockets*, Vol. 31, No. 3, May-June 1994, pp. 516–523.
- <sup>15</sup>Kay, R. D., and Netterfield, M. P., “Thermochemical Non-Equilibrium Computations For a Mars Entry Vehicle,” AIAA Paper 93-2841, July 1993.
- <sup>16</sup>Cook, R., Private Communication, 1993.
- <sup>17</sup>Weilmuenster, K. J., and Hamilton II, H. H., “Calculations of Inviscid Flow Over Shuttle-Like Vehicles at High Angles of Attack and Comparisons With Experimental Data,” NASA TP 2103, 1983.
- <sup>18</sup>Weilmuenster, K. J., “High Angle of Attack Inviscid Flow Calculations Over a Shuttle-like Vehicle with Comparisons to Flight Data,” AIAA Paper 83-1798, July 1983.
- <sup>19</sup>Weilmuenster, K. J., and Hamilton II, H. H., “A Comparison of Computed and Measured Aerodynamic Characteristics of a Proposed Aeroassist Flight Experiment Configuration,” AIAA Paper 86-1366, June 1986.
- <sup>20</sup>Weilmuenster, K. J., and Hamilton II, H. H., “Comparisons of Computed and Experimental Surface Pressure and Heating on 70° Sphere Cones,” AIAA Paper 86-0567, January 1986.
- <sup>21</sup>Gnoffo, P. A., “Hypersonic Flows Over Biconics Using a Variable-Effective-Gamma, Parabolized-Navier-Stokes Code,” AIAA Paper 83-1666, July 1983.
- <sup>22</sup>Gnoffo, P. A., “Point-Implicit Relaxation Strategies for Viscous, Hypersonic Flows,” in *Computational Methods in Hypersonic Aerodynamics* (Murthy, T. K. S., ed.), Computational Mechanics Publications, pp. 115–151, Kluwer Academic Publishers, 1991.
- <sup>23</sup>Gnoffo, P. A., “Upwind-Biased, Point-Implicit Relaxation Strategies for Viscous, Hypersonic Flows,” AIAA Paper 89-1972, 1989.
- <sup>24</sup>Gnoffo, P. A., “An Upwind-Biased, Point-Implicit Relaxation Algorithm for Viscous, Compressible Perfect-Gas Flows,” NASA TP 2953, February 1990.
- <sup>25</sup>Gnoffo, P. A., “Code Calibration Program in Support of the Aeroassist Flight Experiment,” *Journal of Spacecraft and Rockets*, Vol. 27, No. 2, March-April 1990, pp. 131–142.
- <sup>26</sup>Weilmuenster, K. J., and Gnoffo, P. A., “Aeroassisted Flight Experiment Aerodynamic Characteristics at Flight Conditions,” *Journal of Spacecraft and Rockets*, Vol. 27, No. 6, November-December 1990, pp. 684–686.
- <sup>27</sup>Thompson, R. A., and Gnoffo, P. A., “Application of the LAURA Code for Slender Vehicle Aerothermo-  
dynamics,” *Journal of Spacecraft and Rockets*, Vol. 29, No. 1, January-February 1992, pp. 16–23.
- <sup>28</sup>Weilmuenster, K. J., Gnoffo, P. A., and Greene, F. A., “Navier-Stokes Simulations of Orbiter Aerodynamic Characteristics Including Pitch Trim and Bodyflap,” *Journal of Spacecraft and Rockets*, Vol. 31, No. 3, May-June 1994, pp. 355–366.
- <sup>29</sup>Gnoffo, P. A., Weilmuenster, K. J., and Alter, S. J., “Multiblock Analysis for Shuttle Orbiter Reentry Heating from Mach 24 to Mach 12,” *Journal of Spacecraft and Rockets*, Vol. 31, No. 3, May-June 1994, pp. 367–377.
- <sup>30</sup>Roe, P. L., “Approximate Riemann Solvers, Parameter Vectors, and Difference Schemes,” *Journal of Computational Physics*, Vol. 43, October 1981, pp. 357–372.
- <sup>31</sup>Harten, A., “High Resolution Schemes for Hyperbolic Conservation Laws,” *Journal of Computational Physics*, Vol. 49, No. 2, February 1983, pp. 357–393.
- <sup>32</sup>Yee, H. C., “On Symmetric and Upwind TVD Schemes,” NASA TM 88325, 1986.
- <sup>33</sup>Gnoffo, P. A., Gupta, R. N., and Shinn, J., “Conservation Equations and Physical Models for Hypersonic Air Flows in Thermal and Chemical Nonequilibrium,” NASA TP 2867, February 1989.
- <sup>34</sup>Gnoffo, P. A., Hartung, L. C., and Greendyke, R. B., “Heating Analysis for a Lunar Transfer Vehicle at Near-Equilibrium Flow Conditions,” AIAA Paper 93-0270, January 1993.
- <sup>35</sup>South, Jr., J. C., “Calculation of Axisymmetric Supersonic Flow Past Blunt Bodies with Sonic Corners, Including a Program Description and Listing,” NASA TN D-4563, May 1968.
- <sup>36</sup>Brauer, G. L., Cornick, D. E., and Stevenson, R., “Capabilities and Applications of the program to Optimize Simulated Trajectories (POST),” NASA CR 2770, February 1977.
- <sup>37</sup>Braun, R. D., Powell, R. W., Cruz, C. I., Gnoffo, P. A., and Weilmuenster, K. J., “Six Degree-of-Freedom Atmospheric Entry Analysis for the Mars Pathfinder Mission,” AIAA Paper 95-0456, January 1995.
- <sup>38</sup>Sutton, K., and Graves, R. A., “A General Stagnation-Point Convective Heating Equation for Arbitrary Gas Mixtures,” NASA TR R-376, November 1971.

Table 1 - Trajectory Points

$V_\infty$ m/s	$\rho_\infty$ , kg/m <sup>3</sup>	$T_\infty$ , K	$T_{wall}$ , K	$h$ , km	$M_\infty$	$Re_{D,\infty} 10^{-6}$	$\eta$	$\gamma$	comment
7623.	$9.41 \cdot 10^{-6}$	139.5	1600.	69.7	39.3	0.017	-	-	-
7407.	$9.48 \cdot 10^{-5}$	151.7	1600.	50.6	36.7	0.158	-	-	-
6592.	$3.24 \cdot 10^{-4}$	162.0	2000.	40.7	31.6	0.460	-	-	max. htg.
5596.	$7.91 \cdot 10^{-4}$	152.2	2000.	31.4	27.7	0.992	-	-	-
4862.	$1.16 \cdot 10^{-3}$	176.8	2000.	28.5	22.3	1.149	21.4	1.0938	max. Q
4521.	$1.28 \cdot 10^{-3}$	179.0	2000.	26.7	20.9	1.168	-	-	-
3996.	$1.55 \cdot 10^{-3}$	181.6	2000.	24.8	18.3	1.239	19.7	1.1010	-
3515.	$1.85 \cdot 10^{-3}$	183.8	2000.	23.0	16.0	1.290	17.9	1.1105	-
3085.	$2.14 \cdot 10^{-3}$	186.0	2000.	21.5	14.0	1.300	-	-	-
2707.	$2.44 \cdot 10^{-3}$	188.4	2000.	20.2	12.2	1.290	13.9	1.1405	-
2096.	$3.03 \cdot 10^{-3}$	191.5	2000.	18.0	9.4	1.227	10.8	1.1800	-
-	-	-	-	-	6.6	-	8.5	1.2125	-
-	-	-	-	-	2.0	-	2.8	1.3300	-
420.	$7.49 \cdot 10^{-3}$	200.0	300.	8.2	1.9	0.591	-	-	parachute

Table 2 - Perfect Gas Aerodynamic Coefficients

$\alpha$ , deg	$M_\infty$	$C_N$	$C_A$	$C_m$	$C_D$	$C_L$
0.	22.3	0.00000	1.7160	0.00000	1.7160	0.00000
0.	18.3	0.00000	1.7150	0.00000	1.7150	0.00000
0.	16.0	0.00000	1.7122	0.00000	1.7122	0.00000
0.	12.2	0.00000	1.6803	0.00000	1.6803	0.00000
0.	9.4	0.00000	1.6358	0.00000	1.6358	0.00000
0.	6.6	0.00000	1.5970	0.00000	1.5970	0.00000
0.	2.0	0.00000	1.3426	0.00000	1.3426	0.00000
2.	22.3	0.00678	1.7100	-0.00431	1.7091	-0.05290
2.	18.3	0.00563	1.7090	-0.00316	1.7081	-0.05401
2.	16.0	0.00427	1.7040	-0.00179	1.7031	-0.05520
2.	12.2	0.00297	1.6767	-0.00093	1.6757	-0.05555
2.	9.4	0.00421	1.6347	-0.00255	1.6338	-0.05284
2.	6.6	0.00482	1.5960	-0.00322	1.5951	-0.05088
2.	2.0	0.00458	1.3421	-0.00338	1.3414	-0.04226
5.	22.3	0.01573	1.6836	-0.00929	1.6785	-0.13106
5.	18.3	0.01433	1.6809	-0.00804	1.6757	-0.13222
5.	16.0	0.01280	1.6764	-0.00674	1.6711	-0.13335
5.	12.2	0.00922	1.6618	-0.00404	1.6562	-0.13565
5.	9.4	0.01013	1.6278	-0.00599	1.6224	-0.13178
5.	6.6	0.01179	1.5890	-0.00792	1.5839	-0.12674
5.	2.0	0.01147	1.3370	-0.00845	1.3329	-0.10510
8.	22.3	0.02587	1.6260	-0.01572	1.6137	-0.20067
8.	18.3	0.02467	1.6428	-0.01476	1.6302	-0.20420
8.	16.0	0.02323	1.6397	-0.01356	1.6269	-0.20519
8.	12.2	0.01975	1.6265	-0.01117	1.6134	-0.20680
8.	9.4	0.01748	1.6059	-0.01031	1.5927	-0.20618
8.	6.6	0.01852	1.5740	-0.01226	1.5612	-0.20071
8.	2.0	0.01904	1.3289	-0.01383	1.3186	-0.16609
11.	22.3	0.03738	1.6010	-0.02341	1.5787	-0.26879
11.	18.3	0.03647	1.5970	-0.02268	1.5746	-0.26892
11.	16.0	0.03520	1.5935	-0.02192	1.5709	-0.26950
11.	12.2	0.03198	1.5811	-0.01984	1.5581	-0.27029
11.	9.4	0.02855	1.5657	-0.01787	1.5423	-0.27072
11.	6.6	0.02652	1.5460	-0.01733	1.5226	-0.26895
11.	2.0	0.02563	1.3144	-0.01873	1.2951	-0.22564

Table 3 - Real Gas Aerodynamic Coefficients

$\alpha$ , deg	$M_\infty$	$C_N$	$C_A$	$C_m$	$C_D$	$C_L$
0.	31.6	0.00000	1.6984	0.00000	1.6984	0.00000
0.	22.3	0.00000	1.7290	0.00000	1.7290	0.00000
0.	9.4	0.00000	1.6393	0.00000	1.6393	0.00000
0.	1.9	0.00000	1.3079	0.00000	1.3079	0.00000
2.	39.3	0.00749	1.6597	-0.00122	1.6589	-0.05044
2.	36.7	0.00358	1.6796	0.00005	1.6787	-0.05504
2.	31.6	0.00238	1.6943	0.00110	1.6934	-0.05675
2.	27.7	0.00623	1.7138	-0.00344	1.7130	-0.05358
2.	22.3	0.00621	1.7208	-0.00369	1.7199	-0.05385
2.	20.9	0.00557	1.7168	-0.00317	1.7159	-0.05435
2.	18.3	0.00344	1.7141	-0.00110	1.7131	-0.05639
2.	16.0	0.00173	1.6999	0.00066	1.6989	-0.05760
2.	14.0	0.00262	1.6740	-0.00080	1.6730	-0.05580
2.	12.2	0.00322	1.6547	-0.00160	1.6538	-0.05453
2.	9.4	0.00364	1.6382	-0.00218	1.6373	-0.05353
2.	1.9	0.00480	1.3069	-0.00342	1.3062	-0.04081
5.	39.3	0.01852	1.6508	-0.00273	1.6461	-0.12543
5.	36.7	0.01121	1.6595	-0.00290	1.6542	-0.13347
5.	31.6	0.01047	1.6616	-0.00366	1.6562	-0.13439
5.	27.7	0.01451	1.6821	-0.00723	1.6769	-0.13215
5.	22.3	0.01425	1.6877	-0.00735	1.6825	-0.13289
5.	18.3	0.01104	1.6804	-0.00576	1.6749	-0.13546
5.	16.0	0.00996	1.6679	-0.00460	1.6624	-0.13545
5.	14.0	0.00859	1.6563	-0.00414	1.6507	-0.13580
5.	12.2	0.00890	1.6418	-0.00466	1.6363	-0.13422
5.	9.4	0.00971	1.6278	-0.00569	1.6224	-0.13220
5.	1.9	0.01190	1.3027	-0.00846	1.2987	-0.10169
11.	39.3	0.04517	1.5896	-0.01247	1.5690	-0.25897
11.	36.7	0.03592	1.5767	-0.01797	1.5546	-0.26558
11.	22.3	0.03571	1.5954	-0.02202	1.5729	-0.26937
11.	1.9	0.02607	1.2813	-0.01850	1.2627	-0.21890

Table 4 - Aerodynamic Coefficients

Block	Code	type	grid	$\alpha$ , deg	$M_\infty$	$C_N$	$C_A$	$C_m$
1	LAURA	real vis.	61x31x65	0.	22.3	0.00000	1.7290	0.00000
	LAURA	real vis.	81x41x65	0.	22.3	0.00000	1.7290	0.00000
2	LAURA	real vis.	61x31x65	2.	16.0	0.00173	1.6999	0.00066
	LAURA	real vis.	81x41x65	2.	16.0	0.00149	1.7036	0.00100
	LAURA	pressure	81x41x65	2.	16.0	0.00150	1.7016	0.00088
3	LAURA	real vis.	61x31x65	0.	31.6	0.00000	1.6984	0.00000
	LAURA	pressure	61x31x65	0.	31.6	0.00000	1.6944	0.00000
4	LAURA	real vis.	61x31x65	5.	22.3	0.01425	1.6877	-0.00735
	LAURA	perf. inv.	61x31x33	5.	22.3	0.01523	1.6894	-0.00963
	HALIS	perf. inv.	46x37x21	5.	22.3	0.01573	1.6836	-0.00929
5	LAURA	real vis.	61x31x65	5.	16.0	0.00996	1.6679	-0.00460
	LAURA	perf. inv.	61x31x33	5.	16.0	0.01155	1.6788	-0.00616
	HALIS	perf. inv.	46x37x21	5.	16.0	0.01280	1.6764	-0.00674